P1.10 **Four Dimensional Variational (4DVAR) Analysis of the Wind Field based on Doppler LIDAR Data**

Frank Yu *
Department of Environment and Conservation, Western Australia

P.W. Chan
Hong Kong Observatory, Hong Kong

1. INTRODUCTION

The use of 4DVAR analysis in retrieving the three wind components and thermodynamic fields from LIDAR radial velocity data has been investigated by researchers in recent years. Fundamentals of the 4DVAR include a forward large-eddy-simulation (LES) and a backward adjoint integration. The adjoint formulation is particularly complicated due to the required estimation of the gradients of the cost function with respect to all control variables. Two major approaches in constructing 4DVAR have been developed by Chai et al. (2004) and Newsom and Banta (2004). The main difference between the two approaches lies in the number of control variables employed. In Newsom and Banta (2004), the subgrid-scale fluxes of momentum and heat are modeled through theoretical assumptions for turbulent eddy viscosity and thermal diffusivity estimations, rather than treating directly the viscosity and diffusivity as control variables. The advantage of using theoretical subgrid-scale model is that the reduced number of control variable may improve the efficiency of 4DVAR calculation. However, the use of theoretical sub-grid scale model may not be sufficient for resolving the turbulent eddy structures. This is due to the drawback of the inability of using the subgrid-scale model to represent the turbulent field correctly with a single universal constant, especially in strong shear, rotating flow, near topography or transitional regimes (Germano et al., 1991). In order to create a computationally efficient analysis for our purposes, we have followed similar approach as developed by Newsom and Banta (2004). For ensuring the correctness of the retrieved eddy structures, the subgrid-scale model coefficients need to be properly preset before performing LES.

A 4DVAR model has been developed to process the radial velocity data collected by Doppler LIDAR in order to understand the influences of the local turbulent wind field to the air pollutant transportation and the lower atmospheric boundary layer dynamics. In this paper, we implement 4DVAR analysis on the LIDAR data collected at the Hong Kong International Airport (HKIA) with complex terrain in the vicinity. For the simple forward LES model design that is without any further consideration of the terrain effect, the 4DVAR still performs well in revealing the wavy/jump-like airflow features induced by the mountains and analyzes the three components of the complex wind flow efficiently.

The paper is organized as follows. The 4DVAR formulation is described in section 2. Section 3 describes the observations, data filtering scheme and initial configurations required by 4DVAR. The retrieval results and the comparisons with the analysis in Xu and Chan (2007) are presented in section 4. Conclusions of the study are given in section 5.

2. DESCRIPTION OF THE 4DVAR ANALYSIS METHOD

The fundamental idea of the 4DVAR is to fit the prognostic/forward model to the observations. This would rely on the estimation of the cost function to tell whether the ”fitting” is good enough. In our case, the cost function is given as follows.

$$J = Jr + Jd + Js \quad (1)$$

The first term in (1), Jr , is the difference between forward model predicted radial velocity and the LIDAR observations within the specified time window (~3 minutes in our cases). Jd is the divergence penalty term used for suppressing the divergence in the initial field. Js is the smoothing penalty term and it helps to smooth the output a little for easily identifying any possible eddy structures in the retrieved wind field.

Jr and Jd have the forms as taken from Newsom and Banta (2004) whereas the Js is given by

$$Js = \frac{1}{2}\sum_{i,j,k}[w_u(\nabla^2 u) + w_v(\nabla^2 v) + w_w(\nabla^2 w)] \quad (2)$$

* *Corresponding author address:* Frank Yu, Department of Environment and Conservation, 17 Dick Perry Ave., Kensington, WA 6151, Western Australia.
E-mail: frank.yu@dec.wa.gov.au

The weighting factors w_u and w_v are normally set to 0.001 and w_w is set to 0.5. These are guess values for the time being. Further tests are required for determining these weightings empirically. The governing equations and adjoint derivations are summarized in the following subsections (the formulation is similar to Newsom and Banta (2004)).

a. Governing equations

The governing equations are the Boussineq equations for a shallow atmospheric boundary layer:

$$\frac{\partial u_i}{\partial t}+\frac{\partial (u_i u_j)}{\partial x_j}=-\frac{\partial p}{\partial x_i}+\delta_{i3} g\frac{(\theta-\langle\theta\rangle)}{\Theta_{ref}}-\varepsilon_{ijk} f_j u_k-\frac{\partial \tau_{ij}}{\partial x_j}, \quad (3)$$

$$\frac{\partial \theta_1}{\partial t}+\frac{\partial (\theta_1 u_j)}{\partial x_j}+w\frac{\partial \theta_0}{\partial z}=-\frac{\partial \gamma_\theta}{\partial x_j}, \quad (4)$$

$$\frac{\partial u_j}{\partial x_j}=0, \quad (5)$$

Here x_i's are the Cartesian components of the position vector $\mathbf{x}=[x,y,z]$, u_i's the Cartesian components of the velocity vector $\mathbf{u}=[u,v,w]$, δ_{ij} the Kronecker delta, ε_{ijk} the permutation tensor, f_j the Coriolis parameter, g the acceleration due to gravity and angled brackets represent averaging on horizontal planes. The pressure p is the non-hydrostatic component of the pressure normalized by the reference density ρ_{ref}. Virtual potential temperature θ is decomposed as

$$\theta(x,y,z,t)=\theta_0(z)+\theta_1(x,y,z,t), \quad (6)$$

where subscript 0 refers to the initial base state profile and subscript 1 the dynamic perturbations about the base state. Θ_{ref} is a reference virtual potential temperature and is set to be equal to the virtual temperature at the reference level, namely, the ground. τ_{ij} and γ_θ are the turbulent fluxes of momentum and temperature respectively.

The anisotropic component of the turbulent momentum flux is modeled as

$$\tau_{ij}-\frac{1}{3}\delta_{ij}\tau_{kk}=-2K_m D_{ij}, \quad (7)$$

where D_{ij} is the strain rate tensor,

$$D_{ij}=\frac{1}{2}\left(\frac{\partial u_i}{\partial x_j}+\frac{\partial u_j}{\partial x_i}\right)-\frac{1}{3}\delta_{ij}\frac{\partial u_k}{\partial x_k}. \quad (8)$$

The eddy viscosity K_m can be calculated using a number of different models. There are models based on Troen and Mahrt (1986) and Smagorinsky (1963). The former model is used in this paper. The isotropic component of the turbulent momentum flux $\frac{1}{3}\delta_{ij}\tau_{kk}$ is absorbed into the pressure term.

Similarly, the turbulent flux of virtual potential temperature is modeled as

$$\gamma_\theta=-K_h\frac{\partial \theta}{\partial x_j}. \quad (9)$$

Here the eddy diffusivity K_h is given by

$$K_h=\frac{K_m}{P_{r_t}} \quad (10)$$

where the turbulent Prantle number P_{r_t} is typically set to 0.4.

The requirement that the velocity field remains divergence free, as implied by Eq. (5), is enforced either using a pressure correction method or a Poisson pressure equation. In the pressure correction method, the momentum equations are integrated first giving an estimate of the new velocity field u_i^*. This velocity field will in general not be divergence free. The divergence becomes the source term in the pressure correction equation, which is written

$$\frac{\partial^2 p'}{\partial x_i^2}=\frac{\partial}{\partial x_i}\left(\frac{u_i^*}{\Delta t}\right). \quad (11)$$

This is an elliptic equation, which is solved using the BiCGstab matrix equation solver (Nocedal, 1980; Liu and Nocedal, 1989). The resulting pressure correction fields are then used to correct the pressure and velocity fields.

The pressure Poisson equation is written as

$$\frac{\partial^2 p}{\partial x_i^2} = \frac{\partial}{\partial x_i}\left(\frac{u_i}{\Delta t} - \frac{\partial (u_i u_j)}{\partial x_j} + \delta_{i3} g \frac{(\theta - \langle\theta\rangle)}{\Theta_{ref}} - \varepsilon_{ijk} f_j u_k - \frac{\partial \tau_{ij}}{\partial x_j}\right) \quad (12)$$

This equation is solved before the momentum equations, to give a pressure field, which, when used to calculate the pressure gradient in the momentum equations ensures that the velocity field at the end of the next time step remains divergence free. The pressure Poisson equation is used in the 4DVAR wind retrieval for the following selected cases in this paper.

b. Adjoint model equations

The 4DVAR procedure uses an adjoint method to minimize the cost function J. The adjoint equations are derived by requiring that the first variation of the Lagrangian L with respect to all variables vanishes for $t > 0$. For conciseness, we present the adjoint equations for the first-order Adam-Bashforth time integration scheme (Shampine and Gordon, 1975) as an example. For the first-order in time scheme, the Lagrangian is defined as

$$L = J + \sum_{n=0}^{N-1} \sum_{r} [\tilde{u}_i^{n+1}(u_i^{n+1} - u_i^n - \Delta t F_i^n) + \tilde{\theta}^{n+1}(\theta^{n+1} - \theta^n - \Delta t G^n) + \Delta t \tilde{p}^{n+1} P^n] \quad (13)$$

Here $\tilde{u}$, $\tilde{\theta}$ and $\tilde{p}$ are the adjoint variables corresponding to u, θ and p respectively, and Δt is the time step. The functions F^n, G^n and P^n are essentially the right hand sides of the forward model equations with all variables evaluated at the n^{th} time step. For details of the adjoint formulations, reference may be made to the appendix in Newsom and Banta (2004). The current 4DVAR uses the adjoint equations for the second-order Adam-Bashforth scheme that are derived analogously as for the first order scheme.

3. OBSERVATIONS AND DATA QUALITY CONTROL

The current version of 4DVAR takes sounding data directly as the initial mean field over the model domain. Two cases, 00:16 UTC, 8 March 2006 (CASE 1) and 16:14 UTC, 17 April 2006 (CASE 2) are analyzed here. Both cases use data from the 0, 1 and 4.5 degrees Plan-position Indicator (PPI) scans of the LIDAR at HKIA. Several Range-height Indicator (RHI) scans obtained during the different azimuthal angles in the PPI scans are also included to take as much data as possible for 4DVAR assimilation. Low elevation angle scans at the south-eastern side of the domain are mainly obstructed by the high raised terrain. LIDAR scans in both cases selected start normally from around the north and end at around 315° azimuthal angle by leaving a ~45° empty zone without data to the north of the LIDAR due to blockage by the Air Traffic Control Tower near the LIDAR.

The radionsode data at 00 UTC and 12 UTC are used for the two cases respectively (not shown). In the first case, 8 March, the prevailing wind direction below 1000 m level is easterly veering to south-easterly while going vertically aloft. Between 700 m and 300 m levels, the temperature profile has a stable inversion layer (not shown). In the second case, 17 April, we have only the 12 UTC radiosonde data available which also shows an easterly wind at lower level and south-easterly at upper level below 1000 m level. There is also a shallow temperature inversion layer sitting in between 750 m and 600 m levels (not shown). The presence of stable layers in the lower atmosphere may favour the occurrence of terrain-disrupted airflow in the vicinity of the airport.

The LIDAR at HKIA was installed on top of a 50 m high building near the centre of the airport in order to get a clear view for the scanning beams. However, due to the surrounding high raised complex terrain, appropriate data quality controls are required for removing noises and hard target returns. Basically, in these cases, data with signal-to-noise ratio (SNR) < -13dB are not included for assimilation. More comprehensive data filtering schemes provided by HKO (Chan et al. 2006) are also applied to smooth out the spikes and the discontinuity of the gate measurements along the scanning beam is also implemented.

4. WIND FIELD RETRIEVALS

Wind fields are retrieved by 4DVAR assimilating LIDAR data within 3 minutes time window centred at 00:16 UTC of CASE 1 and 16:14 UTC of CASE 2. The output at the centre of time window is considered as the optimal retrieval by 4DVAR. The LIDAR is situated at the centre of the analysis domain (as shown in, for instance, Figure 1(a)).

In CASE 1, the retrieval shows a wave-like feature near the north-eastern corner of the domain (see the variation of the colour contours for vertical velocity at the north-eastern part of Fig. 1(a)). The amplitude of the wave-like feature is smaller than the similar retrieval result in Xu and Chan (2007) (later mentioned as XC07). The wave-like feature shown in figure 2(b) of XC07 (which does not appear at the same location as the wave feature shown in Fig. 1(a)) is rather close to the LIDAR location and the wave patterns are easily identified with variation of vertical velocity. The difference in the retrieval results is possibly due to

the difference in the way that LIDAR data are assimilated into the models and the different smoothing methods as applied to the data. The 4DVAR model used in XC07 interpolates LIDAR data to the model grid points which seems to smooth the data well. On the contrary, the 4DVAR used here weights the model output to the LIDAR data locations without any interpolation. As a result, the output wind field turns out to be nosier but may be more realistic (to be studied further in future research).

Wave structures are also retrieved both at the centre and the western side of LIDAR. More distinct wave-like patterns appears at the south-western part of Fig. 1(a) in parallel to the one described above. At the centre of the analysis domain near the LIDAR location, the retrieved wind pattern is even noisier. This may be due to the existence of the airport buildings or the data voids in the LIDAR scans. The issue would be studied further in future research. From the vector plot, it is seen that the flow is diverted when approaching the central area of the analysis domain.

A cross sectional cut (indicated as a red dash line in Fig. 1(a)) similar to that in XC07 is made (Fig. 1(b)), Waves could be seen downstream of the terrain. Moreover, there is a similar decrease in the magnitude of the horizontal wind as shown in XC07 in the first several hundred metres above the sea level just downwind of the hill. It is also noted that the curvature of the wind flow at the terrain area is quite flat which is possibly affected by the inability of the 4DVAR without taking terrain effect into consideration. When comparing Fig. 1(b) with Figure 2(c) in XC07, the upper level wind shear appears in Fig. 1(b) but is not seen in XC07. This is because 4DVAR here has taken most of the radiosonde observed wind profile as the mean wind in the model whereas no vertical wind shear seems to be assumed in the mean wind profile for all vertical layers in XC07.

From the 100-m level 2D horizontal wind speed plot (Fig. 1(c)), the magnitude in speed agrees well with that shown in XC07. At about 315° azimuth near the centre of the analysis domain in Fig. 1(c), there exists a sharp difference in contour colour separating high and low wind speed zones. This is mainly caused by the difficulty of the 4DVAR data assimilation method in analyzing the wind in the LIDAR data void area. Large magnitude in horizontal wind component is found to appear at the north-western side of the LIDAR and just downwind of the hill at the eastern side of the LIDAR as well. The accuracy of the winds retrieved in these areas would be studied further in future research.

CASE 2 is similar to CASE 1 but with higher elevated stable layer, slight difference in wind direction and lower wind speed shear below 1000 m level. A clear wave-like feature appears at the centre of the analysis domain with the cross sectional cut indicated by a red dash line (Fig. 2(a)). At the downstream of Tai Fung Au as mentioned by XC07, there are wave-like features as presented in Figure 3(b) of XC07. The vertical cross cut (Fig. 2(b)) at the centre shows a similar horizontal wind speed pattern as scanned by the RHI (Figure 3(c) in XC07). The locations of the upward motions in Fig. 2(b) agree well with what shown in the Figures 3(d) of XC07. In Fig. 2(c), the 100-m level 2D horizontal wind speed has pretty similar pattern as shown in Fig. 1(c). However, the high speed zone some 5 km east of the LIDAR adjacent to the hill in Fig. 1(a) does not exist due to the difference in the mean wind direction.

5. CONCLUSIONS

The 4DVAR data assimilation technique has shown to be an excellent tool in determining the small scale turbulences and deriving three dimensional wind fields. The current version of 4DVAR is capable of deriving three dimensional wind field efficiently in near real-time. The results for the two cases as shown in the paper have agreed quite well with the analysis done by XC07. The 4DVAR used in this paper turns out to be more realistic in displaying small scale features without smoothing overdone due to data interpolation to model grids. However, this will still require further model validation to be conducted later in future studies.

The 4DVAR analysis would also require further development to include the terrain effect when applied to cases with complex terrain so that a more realistic retrieval of the three dimensional wind fields could be achieved. In addition, better data quality control and filtering scheme are also required in future investigation to suppress the occurrence of noise in the retrieved wind field by maintaining the more salient features of the airflow.

References

Chan, P.W., C.M. Shun and K.C. Wu, 2006: Operational LIDAR-based system for automatic windshear alerting at the Hong Kong International Airport, *12th Conference on Aviation, Range, and Aerospace Meteorology*, American Meteorological Society, Georgia, U.S.A.

Chai T., Lin C.L. and R. K. Newsom, 2004: Retrieval of microscale flow structures from high-resolution Doppler data using an adjoint model. *J. Atm. Sci*., **61**, 1500-1520.

Germano, M., Piomelli, U., Moin, P. and W. H. Cabot, 1991: A dynamic subgrid-scale eddy viscosity model. *Phys. Fluids*, **A 3 (7)**, 1760–1765.

Liu, D. and Nocedal, J., 1989: On the limited memory method for large scale optimization. Math. *Programming B*, 45 (3), 503-528.

Newsom, R. K. and R. M. Banta, 2004: Assimilating Coherent Doppler Lidar Measurements into a model of the atmospheric boundary layer. Part I: Algorithm development and sensitivity to measurement error. *J. Atm. Ocean. Tech.*, **21**, 1328-1345.

Nocedal, J.,1980: Updating quasi-Newton matrices with limited storage. *Math. Computation,* 35, 773-782.

Sampine L. F. and M.K. Gordon, *Computer Solution of Ordinary Differential Equations: the Initial Value Problem*, Freeman, 1975.

Smagorinsky, J. 1963: General circulation experiments with the primitive equations, I. The basic experiment. *Mon. Weath. Rev*. **91**, 99-164.

Troen, I. and L. Mahrt, 1986: A simple model of the atmospheric boundary layer: Sensitivity to surface evaporation. *Bound. –Layer Meteor*, **37**, 129-148.

Xu, X., and P.W. Chan, 2007: Retrieval of 3D wind field from LIDAR velocity data. *14th Coherent Laser Radar Conference*, Snowmass, Colorado, USA, 8-13 July 2007.

FIG. 1. 4DVAR retrieved wind field at 00:17 UTC on 08 March 2006. (a) The retrieved 2D wind field at 500-m level. The colour contours represent vertical velocity (m/sec). (pink ellipses indicate the wave-like features.) (b) is the vertical cross sectional cut along the red dash line show in (a). Projected wind component is shown in vectors (vertical velocity x 10). Vertical velocity (original value) is in line contours and horizontal wind magnitude in color contours. (c) is the 100-m level horizontal wind component in magnitude.

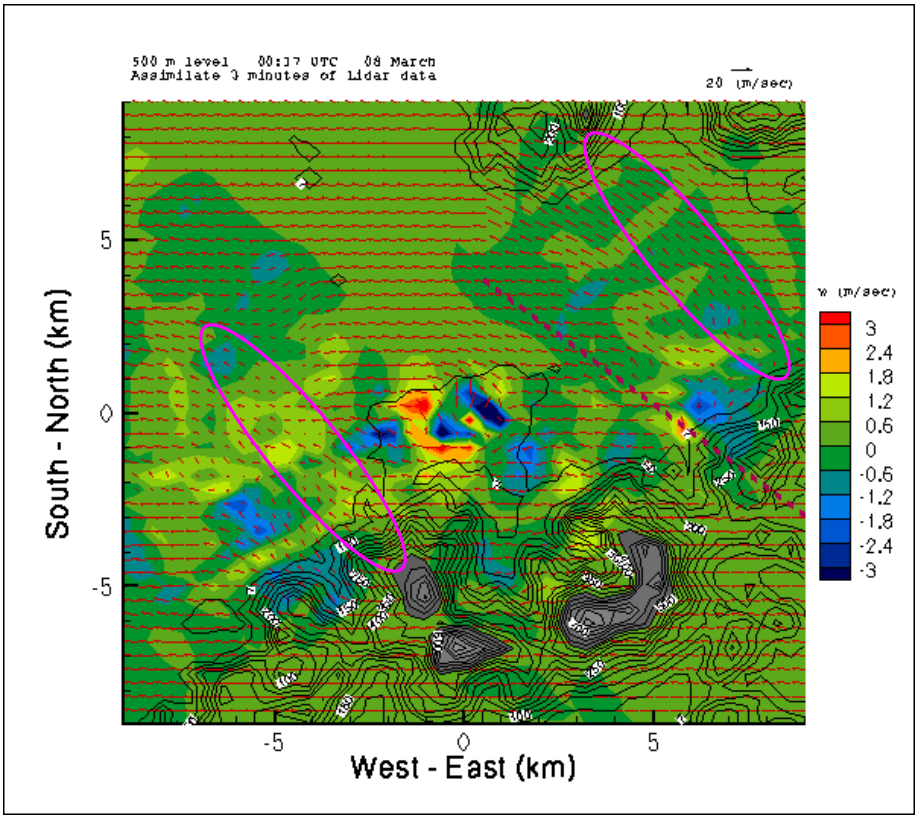

(a)

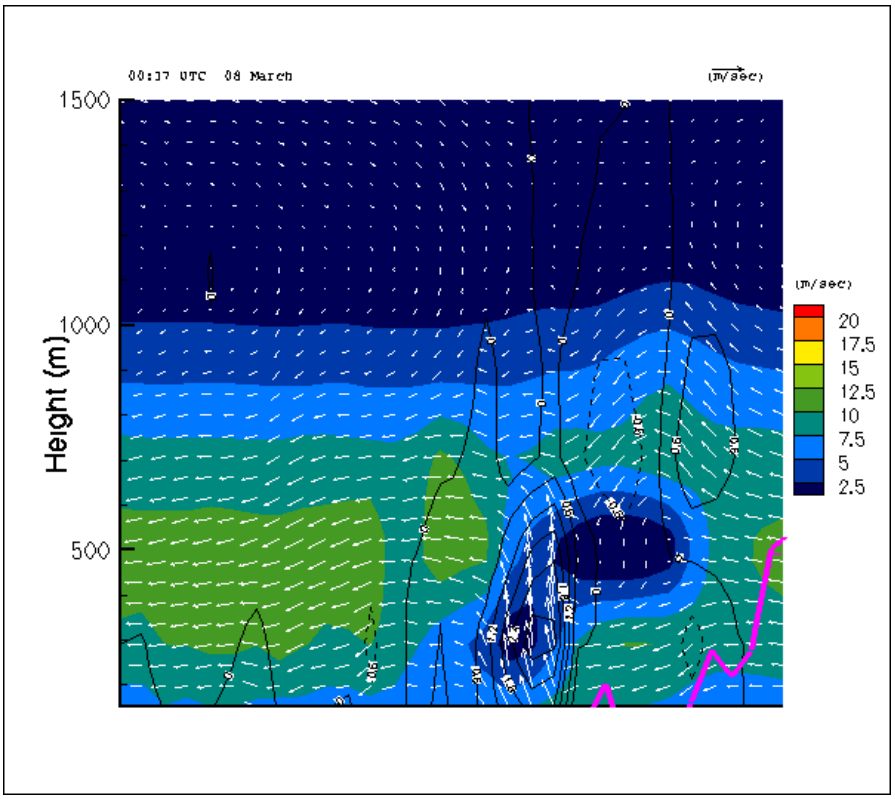
00:17 UTC 08 March
(m/sec)
1500
1000
500
Height (m)
(m/sec)
20
17.5
15
12.5
10
7.5
5
2.5

(b)

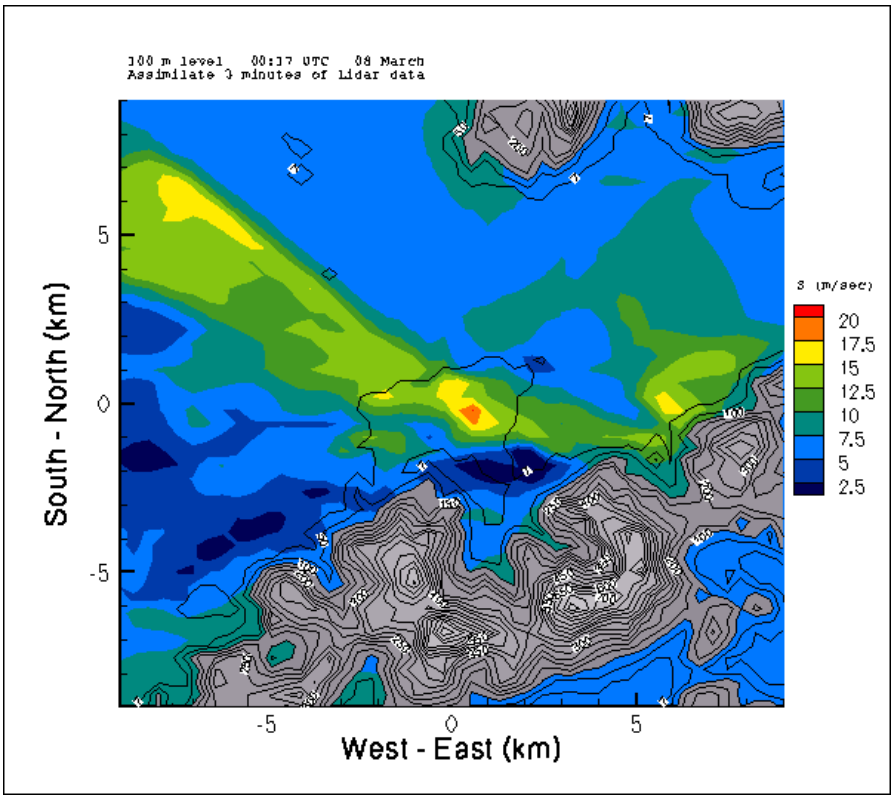
100 m level 00:17 UTC 08 March
Assimilate 3 minutes of Lidar data
5
0
-5
South - North (km)
-5
0
5
West - East (km)
S (m/sec)
20
17.5
15
12.5
10
7.5
5
2.5

(c)

FIG. 2. Same as FIG. 1 but for 16:14UTC on 17 April 2006.

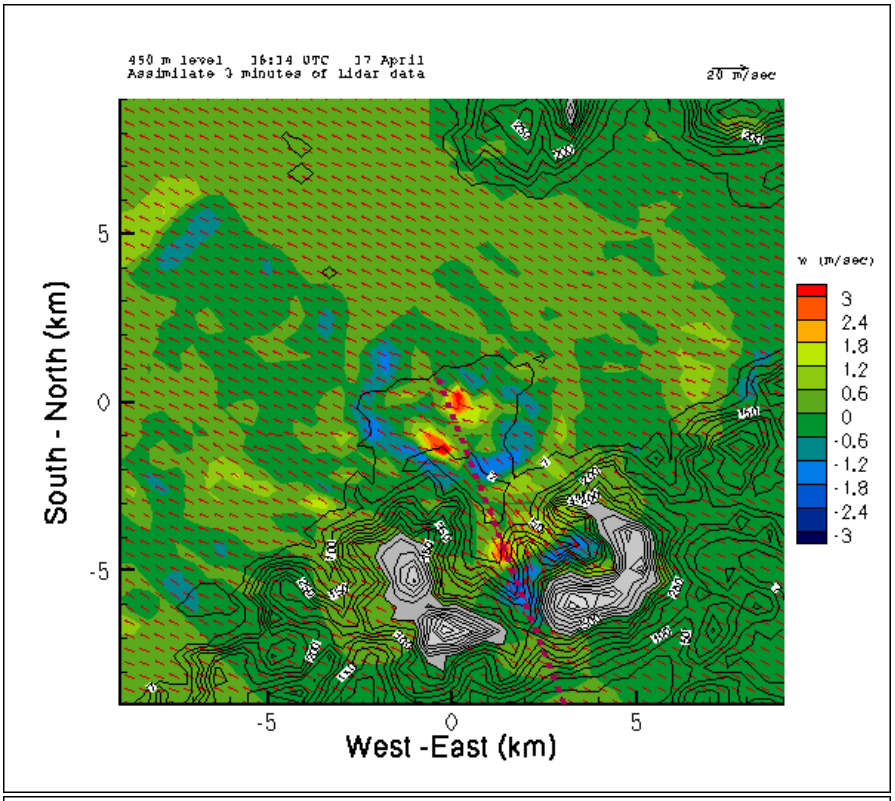

(a)

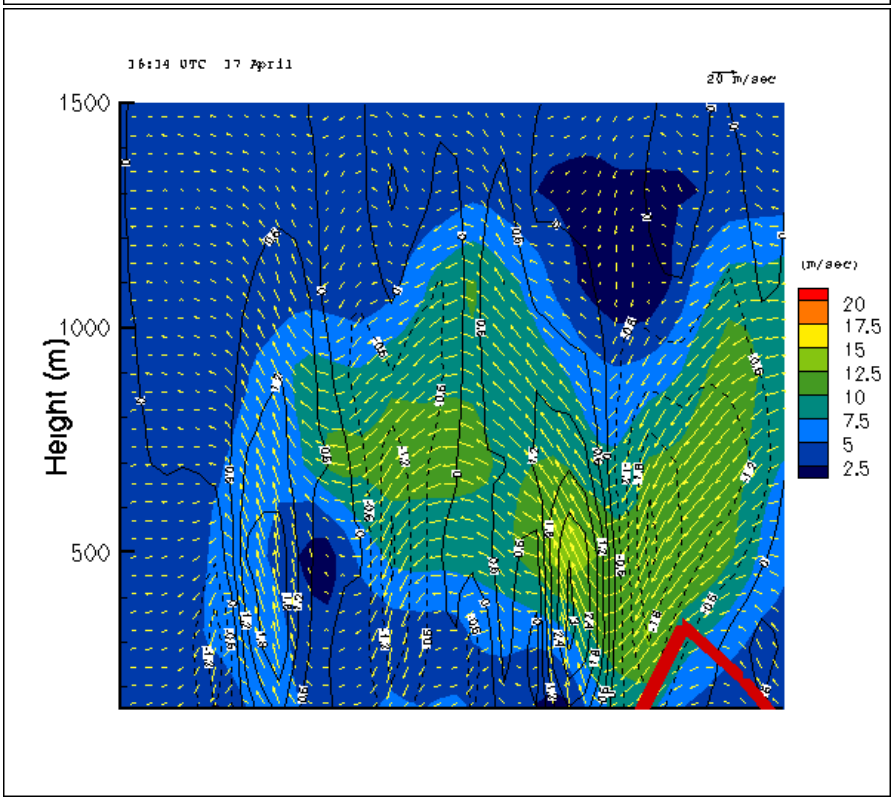

(b)

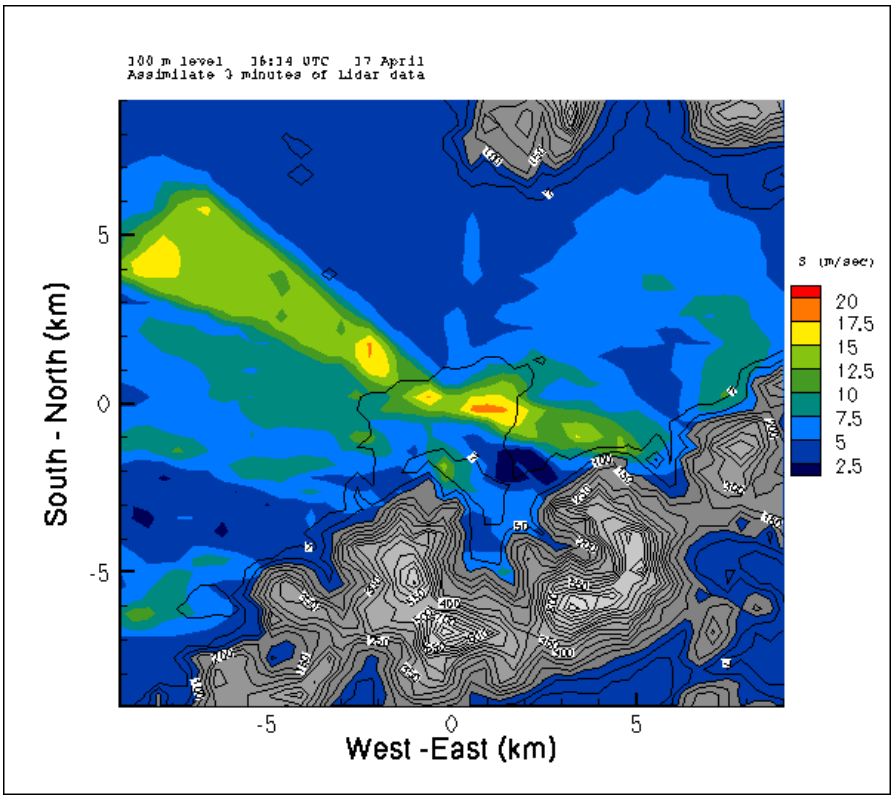
100 m level 16:14 UTC 17 April
Assimilate 3 minutes of Lidar data
South - North (km)
West -East (km)
5
0
-5
-5
0
5
S (m/sec)
20
17.5
15
12.5
10
7.5
5
2.5

(c)